IEEE Photonics Journal
An IEEE Photonics Society Publication

Open Access

Tunable Autler–Townes Splitting Observation in Coupled Whispering Gallery Mode Resonators

Volume 8, Number 5, October 2016

Bo Li
Chong Pei Ho
Chengkuo Lee

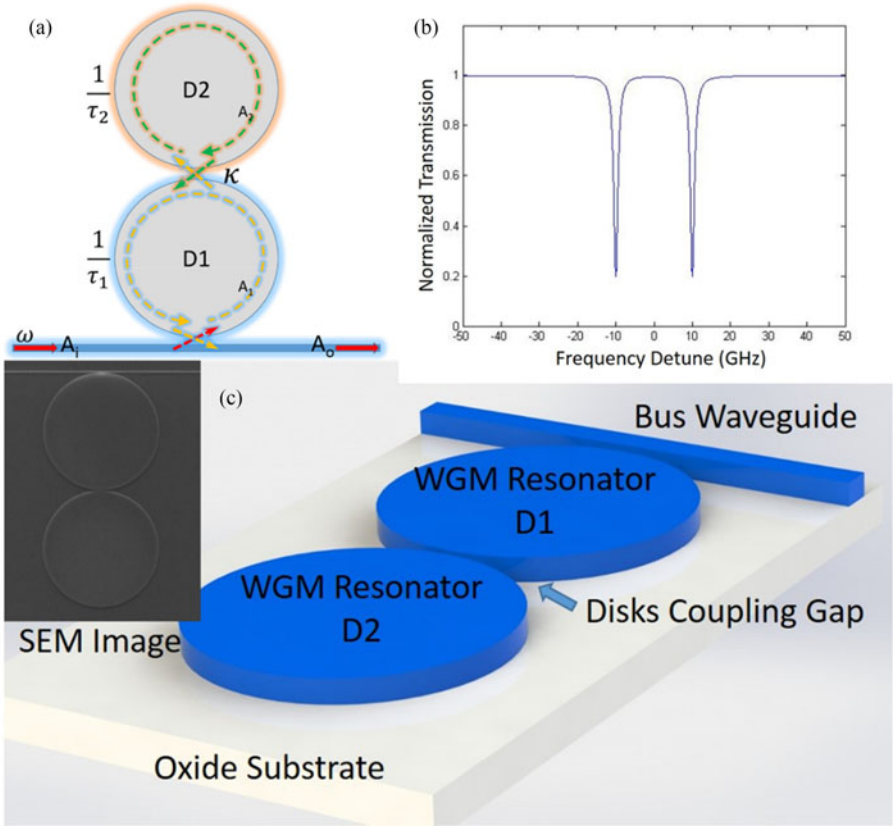

DOI: 10.1109/JPHOT.2016.2601324
1943-0655

Tunable Autler–Townes Splitting Observation in Coupled Whispering Gallery Mode Resonators

Bo Li,[1,2] Chong Pei Ho,[1,2] and Chengkuo Lee[1,2,3]

[1]Department of Electrical and Computer Engineering, National University of Singapore, Singapore 119077, Singapore
[2]NUS Suzhou Research Institute (NUSRI), Suzhou Industrial Park, Suzhou 215123, China
[3]Graduate School for Integrative Sciences and Engineering, National University of Singapore, Singapore 119077, Singapore

DOI:10.1109/JPHOT.2016.2601324

Manuscript received April 1, 2016; revised July 25, 2016; accepted August 10, 2016. Date of publication August 19, 2016; date of current version September 20, 2016. This work was supported in part by the Academic Research Committee Fund MOE2012-T2-2-154 (Monolithic Integrated Si/AlN Nanophotonics Platform for Optical NEMS and OEICs); in part by the National University of Singapore under Grant R-263-000-A59-112; in part by the National Research Foundation (NRF), Singapore, under NRF-CRP15-2015-02 Program "Piezoelectric Photonics Using CMOS Compatible AlN Technology for Enabling The Next Generation Photonics ICs and Nanosensors;" and in part by the National Natural Science Foundation of China under Grant 61474078 at NUS (Suzhou) Research Institute, Suzhou, China. Corresponding author: Dr. C. Lee (elelc@nus.edu.sg).

Abstract: In this paper, we experimentally demonstrated an Autler–Townes splitting (ATS) effect in a cascaded optical whispering gallery mode resonator system. Although electromagnetically induced transparency (EIT) has been investigated as an interesting Fano resonance in the recent decades, the critical resonance matched condition of a high-quality factor resonator and a low-quality factor resonator makes EIT difficult to realize and hardly tunable. In contrast, ATS requires relatively simple system configurations, and the effect can be preserved over a large tuning range. In our approach, a theoretical model based on coupled mode theory is developed, and the methodology of creating and controlling the ATS modes is demonstrated. In our experiment, the optical resonators have a loaded quality factor of about 3×10^5 and cascaded in a strong coupling condition. For the experimental demonstration, a thermo-optical mechanism is utilized to control the splitting modes in our system. The asymmetric shape of a splitting resonances shift has a perfect fit with the theoretical calculations and numerical modeling results. Utilizing the precise tenability of splitting modes, the ATS has an extra degree of freedom to perform resonance tuning, which has become an ideal method to overcome the current detection limit.

Index Terms: Autler–Townes splitting (ATS), coupled disk resonators, tunable photonics, thermo-optical effect.

1. Introduction

The coherent interaction between two resonance photons always results in a transparent window in photonics absorption or transmission spectrum. Some observations of those effects are reported as electromagnetically induced transparency (EIT) [1]–[3] and Autler-Townes splitting (ATS) [4]. EIT is known as a result of Fano interference between two resonance pathways and has received numerous research interests in last decades, especially in optical [5]–[10] and opto-mechanical fields [11]–[12]. The transparent peak displays high quality (Q) factor and slow light effect at the resonance point in the EIT. It brings about many application possibilities such as next generation

optical data storage [13], optical switching [14]–[16] and atomic cooling [17]–[19]. The EIT system requires high Q and low Q resonators, coupled together in a solid state at one particular resonant frequency. Hence, the conditions for an optical system to realize and maintain at EIT state are difficult so that any disturbance will finally migrate the system to other Fano resonance states. This unique criterion brings a lot of challenges in implementing the tunability of the EIT peaks, as well as in assembling the system with flexible photonic [20], [21] and opto-fluidic systems [22], [23]. Moreover, the strong light-matter interaction in the transparent peak reveals narrow operation bandwidth that is hard to be designed for any particular frequencies in absorption optical sensing applications such as bio-particles detections [24]–[26]. On the other hand, ATS, despite having similar transmission spectra as EIT, has only been explored in the field of optical resonator field very recently [27], [28]. This is mainly due to the difficulties in distinguishing between the EIT phenomena and ATS phenomena [29], [30]. ATS is the splitting of energy level that is induced by the optical field mixing. It is usually not associated with interference processes. For the ATS, the resonance mode in the transmission or reflection spectra will split into two associated modes. The spectrum between the two peaks are effectively transparent to the system. It has been used for measuring the electric dipole moment for transaction [31] and spin orbit interaction quantum control [32]. Recently, applications using ATS phenomena in optical field received much greater attention. The splitting resonances help in the detection of particle numbers on an ultra-high Q microresonator [33], and enhancement of label free biosensing using optical microcavity [34]. Attributed to the self-referencing of the two degenerated resonances, the ATS can demonstrate a higher level of sensitivity and resolution because the balancing state of the resonances can eliminate an unexpected disturbance. The effective refractive index (ERI) around the ATS modes can lead to extremely large non-linear coupling between the probe field and other external fields. Hence, the interaction between the optical field and the external matters has been greatly enhanced by the slow light in the transparent window which makes the ATS system a perfect sensing platform. Utilizing the splitting modes, we have an extra degree of freedom to perform resonance tuning. It is an ideal way to overcome the current limitation of optical sensing techniques such as the index shifting and mechanical deformation methods, especially in ultra-low concentration media. Other optical sensing devices such as the Vernier effect, with indirect two-ring cascaded system, usually require a large footprint and wide operating bandwidth, which limits the number of active channels [35]–[38]. Compared with EIT phenomena, the transparent window from ATS is a few orders wider in wavelength, while having similar transmission gain and group delay. Thus, the ATS system has great potential to be implemented in multichannel parallel devices for optical integrated circuits (OIC).

In this scenario, maintenance of the high level balance of the ATS is important in the design principle. However, the non-uniformity in the fabrication process [39] will finally affect the mode splitting configuration of the coupled resonators. Hence, a reconfigurable splitting-mode resonators which can eliminate the fabrication non-uniformity is desirable in the development of ultra-sensitive sensors. In this paper, we investigate theoretically and experimentally a thermo-optically tunable ATS system using two orthogonally coupled whispering gallery mode (WGM) micro disk resonators. The thermos-optically tunable system demonstrates the compact and precise characteristics and is able to perform the individual control of each resonator in the large integrated system. The thermo-optical control of the ATS system dramatically changes the linear absorption and dispersion properties that is reflected in the transmission response.

2. Theoretical Model and Simulations

We begin our investigation by considering a cascaded two level system of coupled optical resonators to generate the ATS. As shown in Fig. 1(a), two WGM disk resonators are cascaded orthogonally to the bus waveguide, which are denoted as D1 and D2 accordingly. The complex intra-cavities field amplitude A_1 and A_2 can be described by the coupled mode theory (CMT) [13], [22], [25]:

$$\frac{dA_1}{dt} = \left(j\omega - \frac{1}{\tau_1} - \frac{1}{\tau_c}\right) A_1 + \sqrt{\frac{1}{\tau_c}} A_i - j\kappa A_2 \tag{1}$$

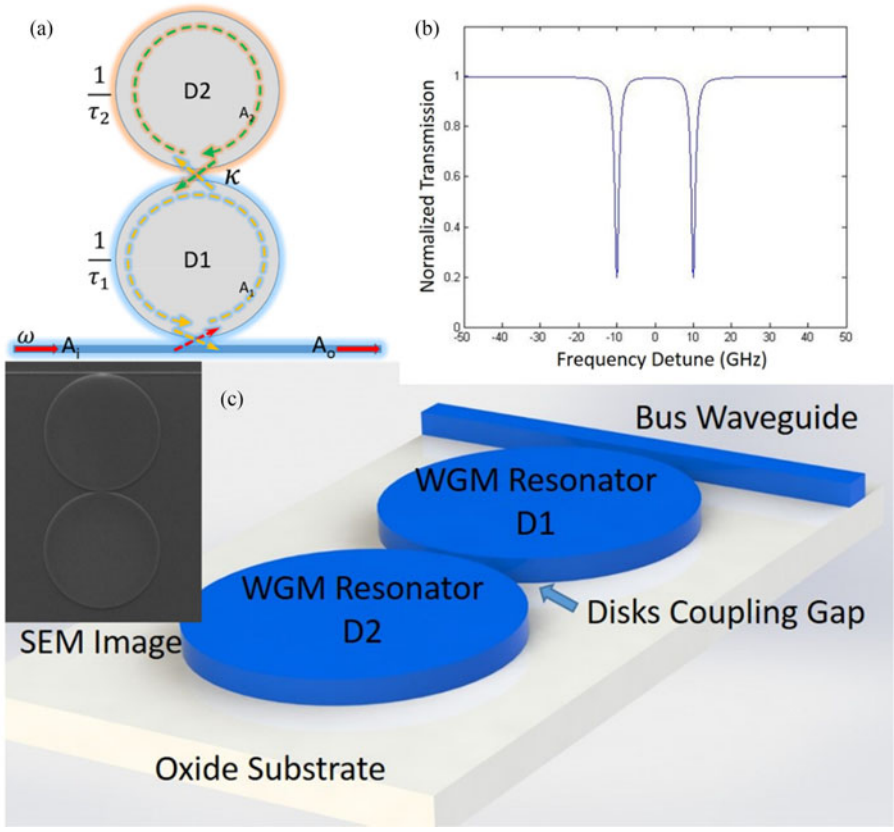

Fig. 1. (a) Schematic of a coupled WGM dual disk resonators; A1 and A2 represent the complex intra-cavities field amplitude of resonator D1 and D2. τ is the photon lifetime constant, and κ represents the coupling coefficient between the D1 and D2. The input light with frequency ω and amplitude A_i is pumped to the system from the left side, and the transmission light with amplitude A_o is collected at the right side. (b) Normalized transmission plot obtained from theoretical equations. The intrinsic Q factor of the disk resonators is based on the measurement data of the device. Hence, the intrinsic decay rate of the disk resonator at 1550 nm is calculated as 1 GHz; the waveguide to disk coupling decay rate is set to be 0.2 GHz; the coupling coefficient κ is set to be 10 GHz. (c) Three-dimensional schematic drawing of the fabricated coupled WGM dual disk resonator and the SEM image.

$$\frac{dA_2}{dt} = \left(j\omega - \frac{1}{\tau_2}\right) A_2 - j\kappa A_1 \tag{2}$$

where ω_0 is the resonance frequency of the disk resonator, probe light ω is propagated through bus waveguide, and the frequency of the probe light will scan across the whole spectrum. τ is the resonance time constant which is related to the quality factor of the resonance by $\omega_0/2Q = 1/\tau$. $1/\tau_c$ represents the decay rate of the coupling between the bus waveguide and the disk resonator D1. The coupling coefficient between the two cascaded disks are denoted as κ in (1) and (2). Under steady-state conditions, the system transfer function can be given by

$$\left|\frac{A_o}{A_i}\right|^2 = \left|1 + j\frac{\omega_1}{2Q_c}\frac{\left(\omega + j\frac{\omega_2}{2Q_2}\right)}{k^2 - \left(\omega + j\frac{\omega_1}{2Q_1} + j\frac{\omega_1}{2Q_c}\right)\left(\omega + j\frac{\omega_2}{2Q_2}\right)}\right|^2. \tag{3}$$

From (3), we can conclude that the overall system transmission spectrum is related to the coupling coefficient κ and intrinsic resonance wavelength ω_1 and ω_2 of the D1 and D2, respectively. Based on our designed cascaded system, in an ideal case, when the two disk resonators have the same

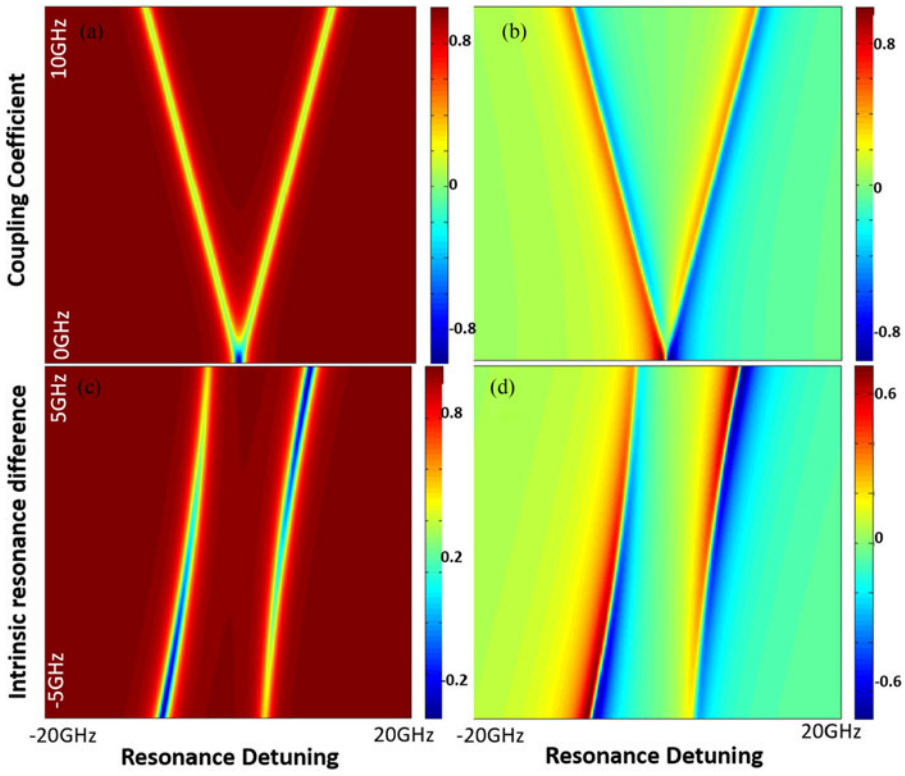

Fig. 2. Normalized transmission plot obtained from (3). The detuning of the input light frequency is from −20 GHz to 20 GHz. The color bar represents the normalized transmission power. (a) and (b) are the transmission plot and phase plot of the system transfer function under $1/\tau = 1$ GHz; $1/\tau_c = 0.2$ GHz; the coupling coefficient κ varies from 0 to 10 GHz. (c) and (d) are the transmission plot and phase plot of the system transfer function under $1/\tau = 1$ GHz. $1/\tau_c = 0.2$ GHz. Coupling coefficient κ changes from 0 to 10 GHz. The intrinsic resonance detuning ω_d varies from −5 to 5 GHz.

intrinsic resonance condition, the transmission port of bus waveguide shows a splitting in resonance with identical line shape and Q factors, as shown in Fig. 1(b), the theoretical plot of a normalized transmission spectra of the cascaded WGM resonator system under the condition that the two disk resonators are identical. In this case, (3) can be rewritten as

$$\left|\frac{A_o}{A_i}\right|^2 = \left|1 - jC\frac{\omega'}{(\omega' + \kappa)(\omega' - \kappa)}\right|^2. \tag{4}$$

The identical disk resonators imply that $\omega_1 = \omega_2, Q_1 = Q_2$ and the strong coupling condition ensure that $Q_c \leq\leq Q_1$. Hence, the two Eigenfrequencies designate the two states of the system centered with the disk resonant frequency ω_0. These two split resonance can be denoted as ω_+ and ω_-.

From (3), the tuning of the ATS can be done by varying the coupling coefficient κ or the disks' intrinsic resonances. The coupling coefficient could be controlled by manipulating the coupling gap distance between the two disk resonators. Fig. 2(a) and (b) illustrate the calculated transmission of the system using (3). The detuning of the input light frequency is from −20 GHz to 20 GHz and the coupling coefficient is tuned from 0 to 10 GHz. The color bar represents the normalized transmission power. Fig. 2(a) depicts that as the coupling coefficient increases, the transmission shows an ATS profile and the two split modes are separated by two times of the coupling coefficient κ. The transparent window between the ω_+ and ω_- become fully transparent when the coupling coefficient is about two times of the disk resonators decay rate. The extinction ratio and the Q factor of the ω_+ and ω_- drop can be observed through the phase change plot of the transmission, as shown in Fig. 2(b).

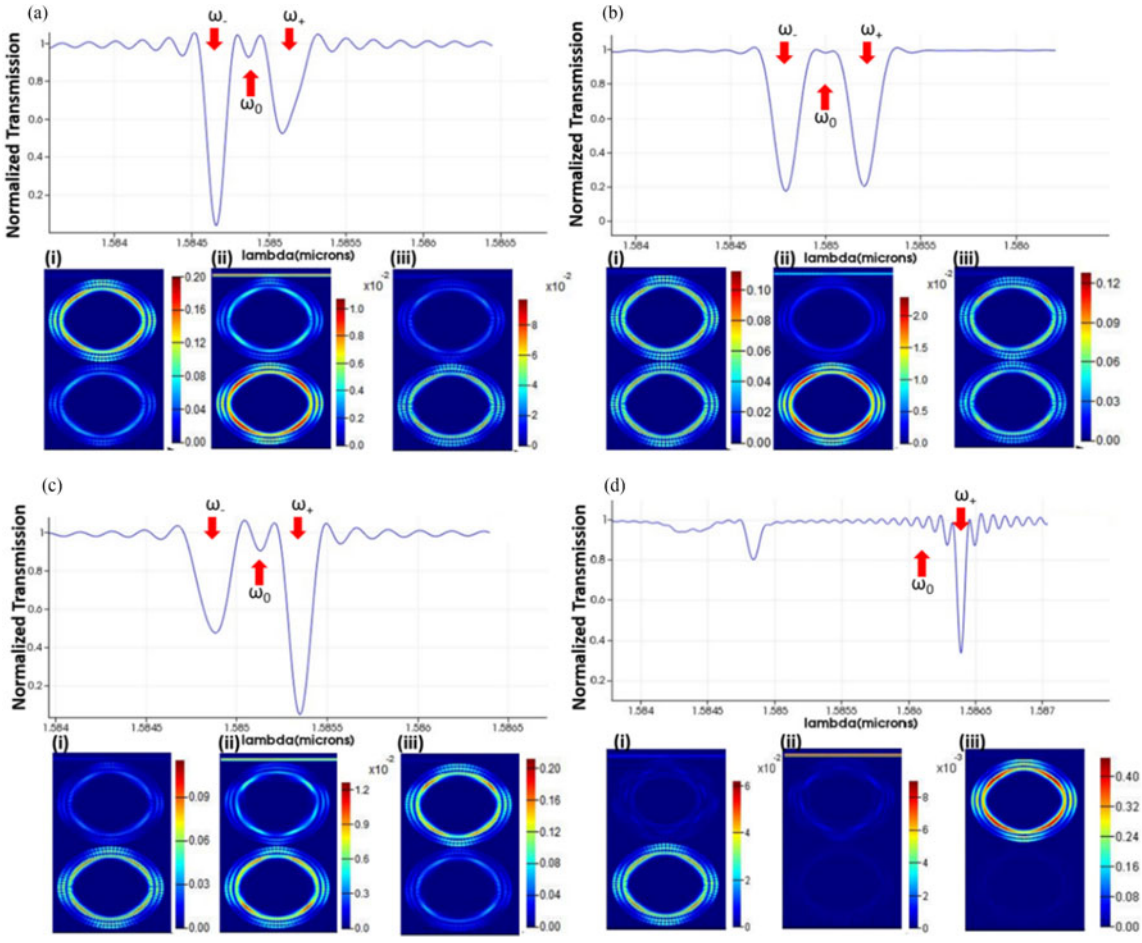

Fig. 3. Three-dimensional FDTD simulations results of coupled WGM disk resonators. (a) Spectra of d1 detuned to the higher resonance frequency. (b) Spectra without detuning. (c) Spectra of d1 detuned to the lower resonance frequency. (d) Spectra of d1 detuned to the threshold frequency. Electrical field distributions of coupled WGM resonator are plotted for each case. (i) ω_+ transmission dip, (ii) ω_0 resonance, and (iii) ω_- dip. In case (ii), the energy scale bar depicts the resonance in the disk and shows two orders of magnitude smaller than cases (i) and (ii), implying a waveguide transmission in the wavelength.

Considering the ATS will only show symmetrical profile when the two disk resonators operate in coherent condition, we can further design the tuning mechanism of coupled optical resonators by varying its intrinsic resonance frequency, such as $\omega_1 + \omega_d = \omega_2$, where the ω_d is the resonance detuning of the D1 resonator. The system transfer function prediction is plotted in Fig. 2(c) and (d). The detuning of the input light frequency is from -20 GHz to 20 GHz and resonance difference is tuned from -5 GHz to 5 GHz. We can observe from the bottom of Fig. 2(a) that the ATS lost its symmetric profile as the resonance conditions of the D1 and D2 differs. The ω_- resonance shows higher extinction ratio than the ω_+ at -5 GHz resonance differences condition. As the resonance differences gradually increase to 5 GHz, the extinction ratio drops on the ω_- and increases on the ω_+. The separation of the ω_- and ω_+ is also modified by the resonance detuning. The ATS modes exhibit the avoid crossing when the detuning is zero in the middle part of the Fig. 3(c) plot. The smallest separation of the transmission dips happens at this condition. However, the transparency level of the modes' separation window is enhanced by the detuning of the disk resonance wavelength. The phase plot shown in Fig. 2(d) illustrates the extinction ratio and the Q factor changes.

The three-dimensional finite-difference time-domain (FDTD) is deployed to characterize our designed ATS system. Fig. 3 shows the numerical simulation results of the cascaded WGM resonators.

The spectrum shown in Fig. 3(b) depicts the zero-detuning case. We can observe two identical Lorentzian line shape bus waveguide transmission as we sweep the probe frequency around the resonance wavelength. The identical linewidth and transmission dip are attributed by the same resonance condition of the two WGM resonators which perfectly matches with the calculated results. The corresponding electrical field plots are shown at the bottom of Fig. 3(b), and the three plotted resonance frequencies are the ω_+, ω_0 and ω_- dips, respectively. In the electric field plots of the dips in Fig. 3(b) (i) and (iii), the resonance E-field in D1 and D2 show an identical profile. The mode energy is equally distributed to both of the coupled WGM resonator.

In Fig. 3(a), the resonance of the D1 is detuned to higher frequency, e.g., a blue shift, where $\omega_1 = \omega_2 - \omega_d$, where ω_1 represent the resonance frequency of D1. The ATS modes show asymmetrical profile. The ω_+ dip has narrower linewidth and higher extinction ratio than the ω_- one which are perfectly matched with the theoretical calculations. The electric field plots in Fig. 3(a) depicts the resonance conditions of the two dips. The mode energy shows the different domination of the WGM resonance power among the two transmission dips. The resonance detune of the D1 enhance the resonance power trapped in it. On the contrary, as shown in Fig. 3(c), as we detune the resonance of the D1 to a lower frequency, the asymmetrical profile is still present; however, the ω_- dip has narrower line width and have higher extinction ratio. The electrical field profiles shown in Fig. 3(c) also show the dominant resonance reverses its position, in accordance with the transmission dip positions. As we continue detuning the intrinsic resonance of D1, the blue shift of the intrinsic resonance will lead the optical energy stored more in blue shift mode and vice versa. As the resonance detuning to a threshold, one of the splitting modes, in this case is ω_-, will disappear as the optical energy is completely shifted, as shown in Fig. 3(d). The dip appears on the lower wavelength region of Fig. 3(d) is the other resonance mode of the coupled disk resonators.

The middle electric field plots (ii) in Fig. 3(a)–(d) depict the electric field profile in the middle of the transparent window. This particular frequency is the intrinsic frequency of the two disk resonators. However, the mode energy in the plot (ii) shows two orders smaller than the other two cases, implies that at this particular frequency, optical filed will couple back to the main bus waveguide and reveals a transparent window. As shown in Fig. 3(b) (ii), at the symmetry condition, the mode energy will go through the bus waveguide and D2 resonator. In the case of the resonance detuning of D1, the energy distribution will split to D1 at the intrinsic resonance wavelength. Detuning direction does not affect the energy distribution graph and so that the plots in Fig. 3(a) (ii) and Fig. 3(c) (ii) are similar. Moreover, the energy level shown in D2 in both the cases is lower than the one shown in plot Fig. 3(b) (ii).

3. Device Fabrication

To experimentally demonstrate the tuning in the coupled resonator ATS system, we fabricated our system on a silicon-on-insulator (SOI) wafer with 220-nm-thickness silicon (Si) device layer, as shown in Fig. 1(c). In the design principle, the same radii of two Si disks ensure the zero-detuning of their resonance. For the fabrication process, the SOI wafer surface will first be patterned with the photonic structures, including disks and waveguides using deep-UV lithography and dry etched using reactive-ion etching (RIE). The bus waveguide is 260 nm in width which ensure the single mode propagation. At the edge of the chips, the waveguide tapers in to 250 nm in width which is designed to match the modes to our taper fiber. The radius of the Si disk is optimized to 5 μm to enhance the thermal efficiency. Next, the whole structure was covered by a silicon dioxide (SiO_2) cladding layer. To meet critical coupling condition and to comply with fabrication capability, the gaps between the waveguides and disks are designed to be 240 nm. To ensure the strong coupling condition between the two resonators, the gap between two disks is set to be 180 nm. From the theoretical model equation (3), the ATS can be tuned with the coupling gap as well as the intrinsic resonance of the resonator. However, the fabrication technique we currently have is only optical lithography method and the best critical dimension control is around 170–190 nm. Hence, the demonstration of disk gap manipulation is beyond our current capabilities. Next, the microheater is deployed on top of the D1 with the following via to connect to the aluminum electrode pad on

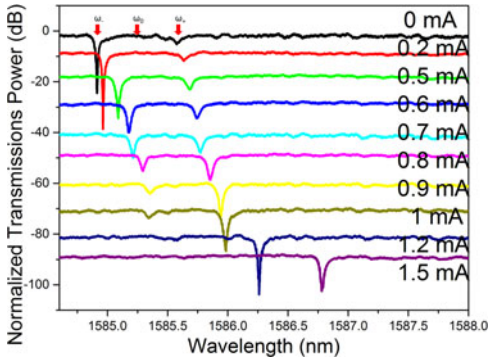

Fig. 4. Measurement results of coupled disk WGM resonators under various bias current addressed to the microheater. The measurement power is normalized to have 10 dB different between every adjacent bias current cases.

top of the chip. Finally, a 1 μm deep trench was etched by Deep-RIE at the end of the waveguide to obtain a smooth coupling sidewall surface for fiber end coupling. The SEM image of fabricated devices is shown in the inset of Fig. 1(c).

4. Results and Discussions

Active manipulation of the ATS resonance of the coupled WGM resonators can be achieved via thermo-optic effect. By varying the ambient temperature, the refractive index of Si can be changed and this induces a shift in the optical resonance frequency. A Cr micro-heater with a rectangular shape of 10 um in length and 4 um in width is deposited on top of D1 with a 600 nm thick of SiO_2 cladding layer. And then the heater is covered by 2 um thick of oxide with aluminum via to connect the aluminum electrical pad on the chip surface. Because of the heat dissipation, the localized temperature for the entire system has a gradient in the longitudinal direction. Hence, the resonance detuning of the D1 and D2 will be reflected in the system transmission spectrum. The measured total resistance of the heater is 148 Ω and controlling power from 0 to 0.33 mW are supplied. The experimental transmission spectrum under different bias current are shown in Fig. 4. These are obtained by monitoring the transmission through the bus waveguide as an external tunable laser is scanned in the frequency range of the optical resonance.

The ATS resonances of the coupled WGM resonator are depicted in Fig. 4. We first observe that in zero-bias condition, the splitting resonance mode is not symmetrical, which is quite similar to the condition shown in Fig. 3(a). This is caused by the non-uniformity of the fabrication process which modifies the intrinsic resonance modes of D1 and D2, resulting in a higher resonance frequency for D1. To demonstrate the tunability of the splitting modes, we first tune the resonance frequency of the resonator to have $\omega_1 = \omega_2$. As we increase the power pumped into the micro-heater from 0 mA to 1 mA, the entire spectrum shifts by 0.427 nm to higher wavelengths due to the increasing temperature and hence the ERI. We also observe a 20 dB intensity difference of the bonding splitting mode dip. As the detuning current reaches 0.8 mA, the transmission dips become symmetric. This implies that the zero-detuning condition is achieved and D1 and D2 have the same resonance frequency. At this stage, the transmission spectra shows two nearly identical Lorentzian lineshape transmission dips (light blue line in Fig. 4). As we further detune the resonance frequency of the D1 beyond the zero-detuning condition, the asymmetric transmission dip shows up again. As described above, instead of the ω_+ dip, the ω_- dip of the ATS mode has a higher extinction ratio. These experimental results matched perfectly with our simulation prediction that the splitting resonance is specifically controllable by detuning on the coupled resonator disk.

In Fig. 4, with the detuning current above 1 mA, we can observe that the transmission dips become the mirror image of the case without thermal control. When we further detune the resonance of

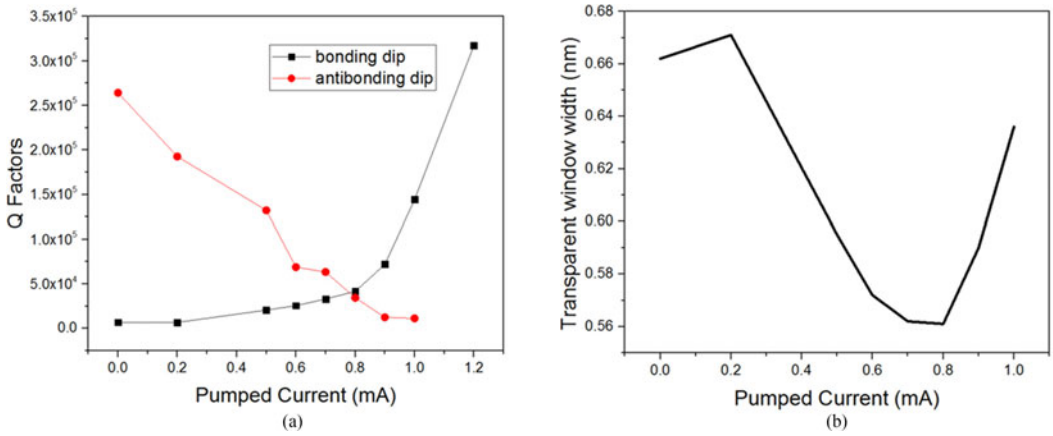

Fig. 5. (a) Relationship of the pumped current and the Q factor of the ATS modes. (b) Relationship of the pumped current and the transparent window width of the ATS modes.

D1 resonator by applying 1.2 mA current, the ATS disappeared. Only one strong dip is left in the transmission spectra. Based on the measurements, the resonance shows the splitting profile below 1mA input and merged resonance beyond this threshold. This is caused by over-detuning of D1 which destroys the coupling condition between the cascaded disks, hence resulting in merged single disk transmission spectrum.

The Q factors of the two ATS dips are plotted against the pumped current in Fig. 5(a). We can see a clear trend of Q factor dropping of ω_+ dip and increasing of ω_- dip as the pumped current increases. The overlapping point represents the balance point for this device which is near 0.78 mA. We can further observe the second order relationship between the transparent window width and the pumped current from Fig. 5(b). The minimum dip separation also happens at the balance point. This can be easily understood via the electric field plot in Fig. 3. In the case of ω_+ dip domination, the optical power is mainly stored in the D1 resonator, where the microheater lays on top. Hence, the ω_+ dip will shift more since D1 experience larger temperature change. In the case of ω_- dip domination, as shown in Fig. 3(c), the optical power is also stored in the D1. Hence, the ω_- dip shifts more in those cases. For the thermo-optical tuning efficiency, resonance shifting and extinction ratio tuning are observed with efficiency of 2.885 nm/mW and 140.16 dB/mW, as shown in Fig. 4, respectively. We obviously found that the extinction ratio tuning is more efficient than the resonance shifting. The heat dissipation shifts the spectra and also causes the intrinsic detune of the two disk resonators. By carefully designing the heat dissipation barrier, e.g., trenches around the D1, between the two disks, we can highly enhance the efficiency of the extinction ratio tuning.

5. Conclusion

In conclusion, an Autler-Townes splitting methodology is demonstrated using the coupled mode theory in a cascaded optical resonator structure. Through the steady state transfer function, precise control of the ATS mode profile and the transparent window is achieved by linearly modifying the resonance frequency of one optical resonator. In our approach, we use two coupled whispering gallery mode disk resonators, deployed with microheater on top of one of the disks. Thermo-optic effect is used to control and manipulate the ATS performance of the proposed coupled disks. It shows efficient reconfiguration of the ATS mode by resonance detuning, which implies that the coupled disks resonators have great potential in ultra-sensitive bio particle sensing as the split modes provide an extra dimension to respond to the sensing signal. In our experiment, the optical resonators are made of Si and have loaded quality factor about 3×10^5. We observe a complete asymmetric ATS tuning and an avoid crossing of the split modes under 0.15 mW of thermal power pump and 0.1 nm transparent window change.

References

[1] K. J. Boller, A. Imamoğlu, and S. E. Harris, "Observation of electromagnetically induced transparency," *Phys. Rev. Lett.*, vol. 66, no. 20, 1991, Art. no. 2593.
[2] S. E. Harris, "Electromagnetically induced transparency," *Phys. Today*, vol. 50, no. 7, pp. 36–42, 1997.
[3] M. Fleischhauer, A. Imamoglu, and J. P. Marangos, "Electromagnetically induced transparency: Optics in coherent media," *Rev. Mod. Phys.*, vol. 77, no. 2, p. 633, 2005.
[4] S. H. Autler and C. H. Townes, "Stark effect in rapidly varying fields," *Phys. Rev.*, vol. 100, no. 2, p. 703, 1955.
[5] M. F. Yanik, W. Suh, Z. Wang, and S. Fan, "Stopping light in a waveguide with an all-optical analog of electromagnetically induced transparency," *Phys. Rev. Lett.*, vol. 93, no. 23, 2004, Art. no. 233903.
[6] D. D. Smith, H. Chang, K. A. Fuller, A. T. Rosenberger, and R. W. Boyd, "Coupled-resonator-induced transparency," *Phys. Rev. A*, vol. 69, no. 6, 2004, Art. no. 063804.
[7] K. Totsuka, N. Kobayashi, and M. Tomita, "Slow light in coupled-resonator-induced transparency," *Phys. Rev. Lett.*, vol. 98, no. 21, 2007, Art. no. 213904.
[8] S. Weis *et al.*, "Optomechanically induced transparency," *Science*, vol. 330, no. 6010, pp. 1520–1523, 2010.
[9] J. Wang, L. Sun, Z. D. Hu, X. Liang, and C. Liu, "Plasmonic-induced transparency of unsymmetrical grooves shaped metal-insulator-metal waveguide," *AIP Adv.*, vol. 4, no. 12, 2014, Art. no. 123006.
[10] H. Li, S. Liu, S. Liu, and H. Zhang, "Electromagnetically induced transparency with large group index induced by simultaneously exciting the electric and the magnetic resonance," *Appl. Phys. Lett.*, vol. 105, no. 13, 2014, Art. no. 133514.
[11] L. Fan, K. Y. Fong, M. Poot, and H. X. Tang, "Cascaded optical transparency in multimode-cavity optomechanical systems," *Nature Commun.*, vol. 6, no. 5850, 2015.
[12] S. A. Tadesse and M. Li, "Sub-optical wavelength acoustic wave modulation of integrated photonic resonators at microwave frequencies," *Nature Commun.*, vol. 5, no. 5402, 2014.
[13] B. Gouraud, D. Maxein, A. Nicolas, O. Morin, and J. Laurat, "Demonstration of a memory for tightly guided light in an optical nanofiber," *Phys. Rev. Lett.*, vol. 114, no. 18, 2015, Art. no. 180503.
[14] M. Albert, A. Dantan, and M. Drewsen, "Cavity electromagnetically induced transparency and all-optical switching using ion Coulomb crystals," *Nature Photon.*, vol. 5, no. 10, pp. 633–636, 2011.
[15] B. D. Clader, S. M. Hendrickson, R. M. Camacho, and B. C. Jacobs, "All-optical microdisk switch using EIT," *Opt. Express*, vol. 21, no. 5, pp. 6169–6179, 2013.
[16] M. J. Lee, Y. H. Chen, I. Wang, and I. A. Yu., "EIT-based all-optical switching and cross-phase modulation under the influence of four-wave mixing," *Opt. Express*, vol. 20, no. 10, pp. 11057–11063, 2012.
[17] C. Genes, H. Ritsch, M. Drewsen, and A. Dantan, "Atom-membrane cooling and entanglement using cavity electromagnetically induced transparency," *Phys. Rev. A*, vol. 84, no. 5, 2011, Art. no. 051801.
[18] A. Schilke, C. Zimmermann, and W. Guerin, "Photonic properties of one-dimensionally-ordered cold atomic vapors under conditions of electromagnetically induced transparency," *Phys. Rev. A*, vol. 86, no. 2, 2012, Art. no. 023809.
[19] M. Bienert and G. Morigi, "Cavity cooling of a trapped atom using electromagnetically induced transparency," *New J. Phys.*, vol. 14, no. 2, 2012, Art. no. 023002.
[20] Y. Chen and M. Li, "Integrated silicon and silicon nitride photonic circuits on flexible substrates," *Opt. Lett.*, vol. 39, no. 12, pp. 3449–3452, 2014.
[21] Y. Chen, H. Li, and M. Li, "Flexible and tunable silicon photonic circuits on plastic substrates," *Sci. Rep.*, vol. 2, no. 622, 2012.
[22] Y. Yang *et al.*, "Optofluidic waveguide as a transformation optics device for lightwave bending and manipulation," *Nature Commun.*, vol. 3, no. 651, 2012.
[23] Y. Yang, L. K. Chin, J. M. Tsai, D. P. Tsai, N. I. Zheludev, and A. Q. Liu, "Transformation optofluidics for large-angle light bending and tuning," *Lab Chip*, vol. 12, no. 19, pp. 3785–3790, 2012.
[24] N. Liu *et al.*, "Planar metamaterial analogue of electromagnetically induced transparency for plasmonic sensing," *Nano Lett.*, vol. 10, no. 4, pp. 1103–1107, 2009.
[25] N. Liu *et al.*, "Plasmonic analogue of electromagnetically induced transparency at the Drude damping limit," *Nature Mater.*, vol. 8, no. 9, pp. 758–762, 2009.
[26] X. J. He, L. Wang, J. M. Wang, X. H. Tian, J. X. Jiang, and Z. X. Geng, "Electromagnetically induced transparency in planar complementary metamaterial for refractive index sensing applications," *J. Phys. D, Appl. Phys.*, vol. 46, no. 36, 2013, Art. no. 365302.
[27] H. Yu, P. Li, M. Chen, H. Chen, S. Yang, and S. Xie, "Analog photonic link based on the Aulter–Townes splitting induced dual-band filter for OCS and the SOI signal processor," *Opt. Lett.*, vol. 40, no. 10, pp. 2225–2228, 2015.
[28] G. Gao *et al.*, "Tuning of resonance spacing over whole free spectral range based on Autler–Townes splitting in a single microring resonator," *Opt. Express*, vol. 23, no. 21, pp. 26895–26904, 2015.
[29] B. Peng, Ş. K. Özdemir, W. Chen, F. Nori, and L. Yang, "What is and what is not electromagnetically induced transparency in whispering-gallery microcavities," *Nature Commun.*, vol. 5, no. 5082, 2014.
[30] T. Y. Abi-Salloum, "Electromagnetically induced transparency and Autler–Townes splitting: Two similar but distinct phenomena in two categories of three-level atomic systems," *Phys. Rev. A*, vol. 81, no. 5, 2010, Art. no. 053836.
[31] M. J. Piotrowicz, C. MacCormick, A. Kowalczyk, S. Bergamini, I. I. Beterov, and E. A. Yakshina, "Measurement of the electric dipole moments for transitions to rubidium Rydberg states via Autler–Townes splitting," *New J. Phys.*, vol. 13, no. 9, 2011, Art. no. 093012.
[32] E. H. Ahmed *et al.*, "Quantum control of the spin-orbit interaction using the Autler–Townes effect," *Phys. Rev. Lett.*, vol. 107, no. 16, 2011, Art. no. 163601.
[33] J. Zhu *et al.*, "On-chip single nanoparticle detection and sizing by mode splitting in an ultrahigh-Q microresonator," *Nature Photon.*, vol. 4, no. 1, pp. 46–49, 2010.

[34] X. Yi *et al*., "Mode-splitting-based optical label-free biosensing with a biorecognition-covered microcavity," *J. Appl. Phys*., vol. 111, no. 11, 2012, Art. no. 114702.
[35] L. Jin, M. Li, and J. J. He, "Highly-sensitive silicon-on-insulator sensor based on two cascaded micro-ring resonators with vernier effect," *Opt. Commun*., vol. 284, no. 1, pp. 156–159, 2011.
[36] V. M. N. Passaro, B. Troia, and F. De Leonardis, "A generalized approach for design of photonic gas sensors based on Vernier-effect in mid-IR," *Sens. Actuators B, Chem*., vol. 168, pp. 402–420, 2012.
[37] M. La Notte and V. M. N. Passaro, "Ultra high sensitivity chemical photonic sensing by Mach–Zehnder interferometer enhanced Vernier-effect," *Sensors Actuators B, Chem*., vol 176, pp. 994–1007, 2013.
[38] X. Jiang, Y. Chen, F. Yu, L. Tang, M. Li, and J. J. He, "High-sensitivity optical biosensor based on cascaded Mach–Zehnder interferometer and ring resonator using Vernier effect," *Opt. Lett*., vol. 39, no. 22, pp. 6363–6366, 2014.
[39] L. Chrostowski, X. Wang, J. Flueckiger, Y. Wu, Y. Wang, and S. T. Fard, "Impact of fabrication non-uniformity on chip-scale silicon photonic integrated circuits," in *Proc. Opt. Fiber Commun. Conf. Opt. Soc. Amer*., 2014, p. Th2A.37.